Particular H 2 O dissolution mechanism in iron-rich melt: Application to martian basaltic melt genesis

Chloé Larre, Yann Morizet, Antoine Bézos, Christèle Guivel, Carole La, Nicolas Mangold

Particular H_2O dissolution mechanism in iron-rich melt: application to martian basaltic melt genesis.

Chloé Larre*[1], Yann Morizet[1], Antoine Bézos[1], Christèle Guivel[1], Carole La[1], and Nicolas Mangold[1]

[1] Laboratoire de Planétologie et Géodynamique (LPG), Université de Nantes, UMR-CNRS 6112, Nantes, Pays de la Loire, FRANCE

* Corresponding author information:

- email contact: chloe.larre@univ-nantes.fr

- tel: +33 (0) 2 5112 5455

Abstract

Martian basalts are different from Earth by their iron-rich abundance with 18 wt % FeO_{tot} in average for Mars upper crust. The H_2O behavior in this atypical melt composition is not well understood. We have synthesized H_2O-bearing martian basaltic glasses (> 15.5 wt % FeO^{ini}) under high pressures (0.5-1.5 GPa) and temperatures (> 1500 °C) conditions. We used Raman spectra to investigate the effect of H_2O as well as the high FeO_{tot} content on the molecular structure of Fe-rich glasses.

Increasing Fe content appears to inhibit the dissolution of H_2O in the melt. We observed the formation of Free OH groups at 3660 cm^{-1} at relatively low H_2O content (1 wt %) in Fe-rich glasses whereas it only appears at high H_2O content (~6.5 wt %) for Fe-poor glasses. We suggest that the Free OH are bonded to Fe^{2+} cations in the melt forming isolating clusters of Fe(OH)2. Such configurations is suspected to induce an increase in the melt polymerization;

however, we did not clearly observe it and further investigation is requested. The major implication of these results is the possibility to form an immiscible hydrated Fe-rich phase that will favor formation of Fe-oxides at Mars surface.

1. Introduction

Many evidences of features related to liquid flows and aqueous phases at the surface of Mars led to the conclusion that water was present in its youth (e.g., [1-3]). To stabilize liquid water at the surface of Mars, an atmosphere thicker and denser than the present one is needed [4-7]. Such primitive atmosphere would either require: 1) volatiles from large extra-terrestrial impacts or 2) volatiles degassing from the interior of the planet through volcanism. Indeed, Mars went through an intense volcanic activity during the Noachian (> 3.7 Ga), resulting in large provinces of igneous basaltic rocks covering the surface [8-12].

The quantification of the volatile fluxes from a planetary mantle to its atmosphere depends chiefly on the volatile content at the source and their respective solubility in the magmatic system. During volcanic eruptions, volatile species such as CO_2, H_2O and SO_2 (for the most important) are degassed into the atmosphere. The behavior of volatile species has been widely investigated for the different terrestrial melt compositions: 1) CO_2, H_2O and SO_4^{2-} for basaltic melt compositions (e.g., [13-16]); 2) CO_2 and H_2O for silica-poor melts (e.g., [17-20]). While studies have focused their work on the volatile solubility in Earth magmatic systems, only few of them have focused on the solubility of volatile elements in martian magmas to constrain the volatile geochemical cycle of Mars. From geochemical modeling and meteorite analyses, estimations of the H_2O in a martian melt have been proposed although values are very scattered from thousands of ppm to 2 wt % H_2O [21 - 23].

Martian interior can be characterized by a wide range of redox conditions: from IW (i.e., Iron Wüstite) to above the QFM buffer (i.e., Quart-Fayalite-Magnetite) [24-26]. Experimental

studies on martian melt were mainly focused on the C behavior under oxidizing and reducing conditions (e.g., [27-30]). Studies of the crystallization sequence for martian melt analogues in presence of H_2O have been proposed [31-33] and the water content determined. However, the H_2O quantification established in those studies cannot reflect the solubility of H_2O in an iron-rich melt. Up to now, there is no experimental study scrutinizing the H_2O dissolution mechanisms for iron-rich glass.

The Raman spectroscopy is a dedicated tool used to investigate qualitatively and quantitatively both crystallized and amorphous materials. Spectroscopic studies were achieved to establish calibrations from Raman spectra in crystallized materials (e.g., [34-36]). Many studies on amorphous materials based on the investigation of CO_2 and S behaviors in a silicate melt have led to subsequent calibrations (e.g. [37-39]). Calibrations to quantify the H_2O in melts by Raman spectroscopy have been proposed by [40-43]. Nonetheless, the behavior of volatile species dissolved in an iron-rich melt prevailing on Mars has been merely addressed by Raman spectroscopy.

In the present study we investigated the behavior of H_2O in an iron-rich melt. We synthesized Fe-rich basalt glasses (15.5 and 23.5 wt % FeO^{ini}) under high-pressure conditions (0.5-1.5 GPa) in equilibrium with a H_2O fluid phase (up to 3 wt % starting H_2O content). The results obtained on Fe-rich glasses are compared to a Fe-poor terrestrial basalt analogue (~ 9 wt %). Experiments at high H_2O content (> 6 wt %) have also been performed on the terrestrial analogue composition. The silicate structure of the obtained glasses has been characterized by Raman spectroscopy. Fe^{2+} and FeO_{tot} (total iron) wet chemistry analyses have been performed in order to discuss the interplay of the Fe coordination state and the H_2O dissolution mechanism. The growth of Free OH molecular groups is observed at very low H_2O content in Fe-rich basaltic glasses and the possible impact of these molecular clusters on element transportation within Mars interiors is discussed.

2. Methods

2.1. Starting Material

Investigated synthetic compositions were prepared in the SiO_2-Al_2O_3-FeO-MgO-CaO-Na_2O system from a mixture of oxides and carbonate (Na_2CO_3). The Fe-rich synthetic basaltic compositions were made according to basaltic rocks identified at the surface of Mars by the Spirit and Curiosity rovers at Gusev and Gale craters, respectively [7, 12]. The two Fe-rich synthetic basaltic compositions were prepared with 15.5 and 23.5 wt % FeO and were referred as GC and CL respectively. A natural Popping Rock $2\pi D43$ glass (i.e., PR, ~9 wt % FeO_{tot}) has also been studied to investigate the H_2O behavior in a terrestrial analogue. The glass chemical compositions are reported in Table 1.

The natural Popping Rock and the synthetic compositions were crushed in an agate mortar for homogenization. Some powders were decarbonated at 850°C for at least 4 hours in a 1 atm furnace (i.e., GCD and PR samples). The wet chemistry results of the starting materials showed that iron is mostly under Fe^{3+} state, Fe^{2+} / ∑Fe at 0.03 and 0.02 for GC and CL starting powders, respectively (see Table 1). Prior to the high pressure experiments, the Fe is almost fully oxidized.

The initial degree of polymerization representing the silicate network tetrahedral units interconnection, calculated according to Brooker et al. [18], is represented by the NBO/T parameter (i.e., Non-Bridging Oxygen per Tetrahedron) in the Table 1. For this calculation, Fe is considered as Fe^{3+} in the mixtures and therefore as a network former cation like Si^{4+} or Al^{3+}. The studied compositions have comparable NBO/T with 0.38, 0.56 and 0.33, for PR, GC and CL, respectively; which represents slightly depolymerized composition.

2.2. High pressure experiments

Pure H_2O was added with a micro-syringe in several proportions (1.0 to 6.5 wt %) at the bottom of a Pt capsule before loading the starting powder. The capsules were welded shut and weighed to check for mass loss before and after the experiment. No evidence for weight loss was observed from the recovered capsules.

The experiments were carried out using piston-cylinder apparatus in the pressure range of 0.5-1.5 GPa (~80 – 120 km in depth for Mars) and 1500 – 1600 °C for temperature range. A ¾ inch talc-pyrex assembly was used. Previous work [44] showed that using talc-pyrex assemblies apply intrinsic fO_2 conditions close to QFM+1 buffer. Temperature was controlled with a B-type thermocouple ($PtRh_6$—$PtRh_{30}$) with an accuracy of ±5°C. The accuracy on pressure was ±10 % and a 10 % friction correction was applied during the experiment. The run duration varied between 1 and 6 hours. Quenching was achieved by cutting off the power and the quench rate was measured and estimated to be above 80°C/s.

2.3. Analytical methods

2.3.1. Spectroscopic methods

The Fourier Transform Infrared spectroscopy (i.e., FTIR) was used for several samples. The acquisitions were acquired with a IR microscope attached to a Nicolet FTIR 5700, with a X15 Cassegrain objective. The analysis conditions were: a white light source, an InSb detector and CaF_2 beamsplitter. Acquisitions were performed in the near IR area between 3000 – 6000 cm^{-1} with a spectral resolution of 4 cm^{-1}. Each sample is an accumulation of 100 repetitive scans. The samples were not polished due to their small sizes. Measurements of the thickness of each glass chips were realized with a digitometer (with an accuracy of $\pm$ 1 µm) to link the absorption to the H_2O content using the Beer-Lambert approximation [13, 14].

We used a Jobin-Yvon Labram HR800 Raman spectrometer equipped with a 532 nm solid-state laser at the Laboratory of Planetology and Geodynamic (LPG, Nantes University, France). The output power was set at 50 mW to prevent sample damage. We used a grating of 1200 grooves/mm corresponding to a spectral resolution of ~0.8 cm^{-1}. The acquisition time was typically 30 sec with 6 repetitive scans. Spectra were acquired in a non-confocal mode with a slit aperture of 200 µm and a spot size estimated ~1 µm in diameter. A X50 Olympus objective was used. At least 5 spectra were acquired on each sample to investigate the homogeneity of the recovered sample with respect to the dissolved H_2O. The studied spectral range was between 200 and 1250 cm^{-1} and between 2600 and 4000 cm^{-1}, covering the area of the silicate network and the H_2O vibrations, respectively.

H_2O dissolved in silicate glasses exhibits Raman vibrations corresponding to the vibrations stretch and bending (ν_1 and ν_2) of H_2O_{mol} and OH^- represented by an envelope with a peak maximum at ~3550 cm^{-1}. A shoulder at 3660 cm^{-1} can be observed and is attributed to Free OH groups vibrations [45-47]. We tested several calibrations to quantify H_2O in glasses: [40, 41, 43]; using the ratio between the HF area (i.e., high frequency) band in the 800 – 1200 cm^{-1} and the H_2O band at 3550 cm^{-1} [40, 43] and the intensity of the same band [41]. Although, these calibrations were not fully tested to quantify H_2O in Fe-rich basaltic glasses; at a given composition, the H_2O content can be compared from one sample to another.

2.3.2. SEM and EPMA analysis

We performed Electron Probe Micro-Analysis (EPMA) and Secondary Electron Microscopy (SEM) equipped with Energy Dispersive Spectroscopy to determine the major elements compositions of our glasses. The SEM analyses were performed with a JEOL JSM 5800LV with a beam current at 5 nA and a voltage at 15 kV, at Institut des Matériaux Jean Rouxel of Nantes (IMN, France).

The EPMA analyses were made using a Cameca SX 100 at IFREMER of Brest (France). A spot size of 10 µm and a beam current at 6 nA were chosen for the glass components. The acquisition time was 10 s on the sample and 5 s on the background. The standards chosen for our analysis were: wollastonite (Si, Ca), corindon (Al), TiMn oxide, andradite (Fe), NiO, albite (Na), forsterite (Mg), apatite (P), orthose (K), Cr_2O_3 oxide. The associated error is on the order of 2 % in relative to the measured value (see Table 2).

We can see in the Table 2, that the PR-3H-6h sample has experienced a strong Fe loss (2.7 wt % FeO_{tot}) during the experiment considering that the FeO_{tot} in the PR composition is ~9 wt %. This Fe-loss has previously been observed [48] and it is known from experimental study that the Fe can form an alloy with the Pt capsule. Even knowing the loss of Fe during experiments, the Fe-enrichment of the capsules has not proven its efficiency either. Then the Fe-loss cannot be accurately controlled in high pressure and temperature experiments. However, all the experiments have experienced depletion with respect to Fe. The following results are then considering the FeO_{tot} after the experiments.

2.3.3. Colorimetric determination of the Fe^{2+} / ∑Fe ratio

The Fe^{2+} / ∑Fe ratios were measured using the colorimetric method of Wilson [49] recently modified by Schuessler et al. [50]. About 3 mg of samples were weighted in 7 mL crystal polypropylene beakers with a precision of 10^{-3} mg and dissolved for 3 days at room temperature in 1 mL of concentrated HF and 1 mL of 0.139 mol. L^{-1} ammonium vanadate (V^{5+}). As the digestion progresses in such low pH solutions, the Fe^{2+} released from the silicate matrix reacts immediately with the V^{5+} to form Fe^{3+} and V^{4+}. This reaction, which prevents any accidental and irreversible oxidation of Fe^{2+} into Fe^{3+} [49], may be reversed if the pH of the solution is raised up to 5. Once the digestions were completed, 5 mL of beryllium sulfate solution (500

g.L^{-1}) was added to the beakers in order to neutralize the excess of HF and breakdown all insoluble fluorides. The final solutions for FeO colorimetric measurement were prepared in volumetric flasks filled with 10 mL of ammonium acetate buffer solution at 500 g.mol^{-1} (to raises pH up to 5), 5 mL of 2:2'-dipyridil solution as the ferrous colorimetric reagent and ultra-pure water to filled up to 100 mL. The $FeO_{tot.}$ analytical solutions were prepared by adding between 5 to 10 mg of hydroxylamine hydrochloride to an aliquot of the ferrous analytical solutions [50]. This strong reducing agent ensure the quantitative reduction of all remaining Fe^{3+} into Fe^{2+}. The colorimetric measurements were made with the UV/VIS spectrophotometer CARY UV500 (Varian). The optical density measurements were done at 525 nm where the ferrous 2.2' -dipyridil complex absorption is maximum [49]. The peaks heights were measured relative to the baseline at 700 nm and the Fe^{2+} / ∑Fe ratios were determined by dividing the absorbance ratios corrected for the procedural blanks. The results of the Fe^{2+} / ∑Fe measurements on the international reference material JB-2 (Fe^{2+} / ∑Fe = 0.78 ±0.005, N=19) are in good agreement with the recommended values (i.e., 0.78, [51]).

3. Results

3.1. Raman spectra

The Raman spectra obtained on H_2O-bearing glasses synthesized at 1 GPa are represented in Fig. 1A. The Raman spectra were treated with Labspec 6© software and a 5-degree polynomial fit which goes through entrenched points (200 – 250 cm^{-1}, ~600, ~800 and > 1150 cm^{-1}) to subtract the baseline is used [41]. The spectra are arranged according to their FeO_{tot}. We distinguish two parts: the HF region 800 – 1200 cm^{-1} and the LF region 200 – 600 cm^{-1}. The 800 – 1200 cm^{-1} region represents the stretching of the silicate network (ν_1). The region between 200 and 600 cm^{-1} in amorphous material is still not well constrained owing to the complexity

of the many vibrations occurring and overlapping together. Previous studies [52] have shown that the LF region is a complex mixture between bending of tetrahedron from the silicate network (e.g., Al, Si, Ti or Fe in tetrahedral coordination) and bending of tetrahedron in relation to cation network modifiers (e.g., Mg, Ca, Na, K and Fe in octahedral coordination). Although in the subsequent discussion, we will address in more detail the HF region, we observe that the LF region is more intense than the HF region for the PR-6Hb and PR-3H-6h, with 4.5 and 2.7 wt % FeO_{tot} respectively. There is an opposite behavior for the Fe-rich synthetic glasses (e.g., GC-3H-6h, GC-H_2O-4h, GCD-3H-6h, CL-3H-6h). In the PR samples (PR-3H-6h and PR-6Hb), the HF region is asymmetric and exhibits three main features: 850, ~1000 and 1050 cm^{-1}. The most intense peak is localized around 1000 cm^{-1}. In the GC samples (GC-H_2O-4h and GCD-3H-6h) peaks at 850 and 1050 cm^{-1} are smoothen but distinguishable. An intense peak around 950 cm^{-1} is present for GC synthetic glasses. Finally, for CL-3H-6h, the HF region shape is almost symmetric with an intense peak centered at 950 cm^{-1}. A Lorentzian-shape peak is observed between the LF and HF region a 670 cm^{-1} for the iron-rich sample CL-3H-6h and the Popping Rock PR-6Hb.

3.2. H_2O quantification by Raman spectroscopy

Raman spectra of glasses synthesized 1 GPa are shown in Fig. 1B in the H_2O vibration region between 3400 and 3700 cm^{-1}. Acquisitions were also performed between 4000 and 4300 cm^{-1} to investigate the possible presence of H_2 at 4135 cm^{-1} [53] but no signal was found. A main broad feature is observed at 3550 cm^{-1}. At 3660 cm^{-1}, we can observe a shoulder only presents for the CL-3H-6h and PR-6H-b samples corresponding to Free OH species.

The quantification of H_2O in our samples was performed using the calibration of Mercier et al. [41] and according to the following equation (1):

(1) $$H_2O\ (wt\ \%) = \frac{I\,H_2O_{tot}}{I\,HF} \times \frac{1}{a}$$

With I H_2O_{tot} the maximum peak intensity at 3550 cm^{-1}, HF the intensity taken at 960 cm^{-1} and *a* the correlation coefficient chosen for a basaltic composition (i.e., 0.26).

Quantifications have been done on at least 5 spectra. The estimated error on the quantification method is ± 0.06 wt % H_2O [41]. Therefore, the H_2O errors mentioned in Table 2 are a combination of 1) the error relative to the H_2O homogeneity in the glass if above the error calibration provided by Mercier et al. [41], 2) the calibration error (0.1 wt %) if H_2O homogeneity is lower than this value.

In Fig. 1B, spectra are normalized according to the concomitant HF peak intensity in Fig. 1A. The PR glass with 4.5 wt % FeO_{tot} dissolves 6.5 wt % H_2O and shows the highest peak at 3550 cm^{-1} (i.e., PR-6Hb). The peak intensity is decreasing towards higher FeO_{tot} contents: for the CL-3H-6h (with 16.0 wt % FeO_{tot}) 0.9 wt % H_2O is recovered. The highest 3550 cm^{-1} peak intensity corresponds to the highest H_2O content.

The derived H_2O contents are reported in Table 2. High water content experiments at 1 GPa have been measured for the PR composition with 4.1 and then 6.5 wt % H_2O dissolved in the melt with 5.7 and 6.5 wt % H_2O^{ini}, respectively (i.e., PR-6H-4h and PR-6Hb). Experiment with 0.9 wt % H_2O^{ini}, at 1 GPa, has been tested for the GC composition (i.e., GC-1H-4h sample). Almost all the H_2O initially added is recovered in the melt: 0.8 wt % H_2O. Experiments with more than 3 wt % H_2O for the synthetic martian basalt compositions were performed at 1 GPa but no quenched glass could be obtained. At 1.5 GPa, 0.8 wt % H_2O is determined in GCD-3H-6h-1.5GPa, with ~3 wt % H_2O^{ini}. Finally, at low pressure 0.9 wt % H_2O is dissolved in the same starting composition (i.e., GCD).

3.3. H_2O quantification by FTIR versus Raman

FTIR spectroscopy has been conducted on several glass samples in order to investigate the applicability of the Mercier et al. [41] calibration on Fe-rich basalts. Not all samples could be

analyzed because of 1) sample size (small glass chips < 1mm); 2) quenched crystals at the rim of the samples. Only pure glass chips with a size > 2 mm have been analyzed: GC-3H-6h, GC-1H-4h, GCD-3H-6h, PR-3H-6h, PR-6H-4h and PR-6Hb. The determination of water content by FTIR follows the Beer-Lambert equation [13, 14]:

(2) $C_{H_2O} = \frac{100 \times MM \times A}{d \times \rho \times \varepsilon}$

Where C is the H_2O^{mol} or OH^- content in wt %, A the height of the band for OH^- (4500 cm^{-1}) or H_2O_{mol} (5200 cm^{-1}), MM the molar mass in g/mol (H_2O or OH), d the thickness in cm, ρ the density in g/L and ε the linear molar absorption coefficient in L/mol/cm.

For PR samples, we used the extinction coefficients derived from Ohlhosrt et al. [54] 0.56 L/mol/cm for both the peak at 4500 and 5200 cm^{-1}. For our Fe-rich we used the extinction coefficient given by Stolper [55] considering that the studied basalts are closer in composition to ours. The molar absorptivity coefficients are 0.98 and 1.76 L/mol/cm for 4500 and 5200 cm^{-1}, respectively.

Glass density measurements were not possible considering the size of our glass chips. It was calculated using the calibration of Schiavi et al. [43]; which takes into account the chemical composition and is applicable to Fe-rich glass compositions.

In Fig. 2, we observe that the H_2O quantified with Mercier et al. [41] provided better correspondence to the FTIR results. At low H_2O content, for Fe-rich glasses, the H_2O quantification by Mercier et al. [41] is close to the 1:1 line. As an example, for the GC-3H-6h sample, 1.4 wt % and 1.5 wt % H_2O are determined by FTIR and Raman, respectively. At higher H_2O content (> 2 wt %), the results are more scattered, but still in reasonable agreement with the FTIR results. For the water-rich sample (PR-6Hb), 6.9 wt % H_2O is determined by FTIR, where 6.5 is calculated by the method of Mercier et al. [41]. There is a strong discrepancy for PR-6H-4h with 4.1 wt % H_2O determined by Raman whereas 6.1 wt % is determined by FTIR.

However, this sample has the highest error bar due to possible heterogeneity in the H_2O distribution with the glass.

In Fig. 2, the calibration provided by Behrens et al. [40] slightly overestimates the water content for Fe-rich glasses at low H_2O content. For GC-1H-4h, 1.1 wt % H_2O is quantified with Raman and 1.0 wt % by FTIR; although 0.9 wt % H_2O was initially added before the experiment. The discrepancy becomes more important at high H_2O content in PR-6Hb glass: 8.1 wt % H_2O by Raman with 6.5 wt % H_2O^{ini}. However, it should be emphasized that the calibration is accurate to 4.7 wt % H_2O; and at higher content, the error in determining the amount of H_2O will be larger.

The calibration established by Schiavi et al. [43] shows good results for low H_2O content in Fig. 2 with 0.7 wt % for GC-1H-4h against 1.0 wt % H_2O by FTIR. However, with increasing H_2O content, there is an increasing deviation with the FTIR results. This difference can be ascribed by the high Fe content of basalts in Schiavi et al. [43] (FeO_{tot}, > 7 wt %) compared to our Fe-poor basalts (< 6 wt % FeO_{tot}).

The comparison provided in Fig. 2 suggests that we can reasonably assess that the Raman calibration established by Mercier et al. [41] is more appropriate to quantify H_2O in our Fe-rich and Fe-poor basaltic glasses. The results from all H_2O quantifications by IR and Raman spectroscopies are reported in the Table S1 (Supporting Information).

4. Discussion

4.1. H_2O content in Fe-rich basalts

Differences between H_2O dissolved in the melt and H_2O^{ini} can be observed for PR samples (Table 2). For 5.7 wt % H_2O added in PR-6H-4h experiment, less than 4 wt % H_2O is dissolved.

For 6.5 wt %, ~6.5 wt % H_2O is recovered in the PR glass. Under these conditions (i.e. 1 GPa), H_2O solubility is close 7 wt % [56]. The difference between initial and final amount of H_2O for PR glasses is explained by the thermodynamic equilibrium of the H_2O species in the liquid and fluid phase [57]; by extension, there is a partitioning of H_2O between the fluid phase and the melt phase.

Some mixtures were not decarbonated and CO_2 was present in the fluid phase during the experiments. However after the experiments, no CO_3^{2-} signal at 1080 cm^{-1} was observed by Raman spectroscopy [37], implying that only hundreds ppm of CO_2 could be dissolved. It is consistent with previous studies that estimated the CO_2 solubility in these iron-rich melt at ~0.3 wt % under oxidized conditions [27, 28].

The presented results in Fig. 1B and Table 2, suggest that increasing Fe content will induce a substantial decrease in the H_2O dissolution. For instance, if we compare the PR-3H-6h and GCD-3H-6h samples with 2.9 and 2.7 wt % H_2O^{ini}, the total H_2O dissolved in the melt is 2.8 and 0.7 wt % H_2O, respectively. For those two experiments made at identical intensive conditions and with no CO_2 present, there is a difference of ~2 wt % between H_2O dissolved and the H_2O initially loaded in the sample charge. The most likely hypothesis to explain this difference is the change in the Fe content: ~13 wt % for GC samples and 5 wt % FeO_{tot} for PR.

We have presented the H_2O dissolved as a function of the FeO_{tot} for 1 GPa experiments in Fig. 3. We observe a decrease of the H_2O content from 6.5 wt % H_2O at 5 wt % FeO_{tot} for PR-6Hb, to less than 1 wt % at 16 wt % FeO_{tot} for CL-3H-6h (see Table 2). Hence, increasing the FeO_{tot} in the melt composition seems to hamper the H_2O dissolution. This trend has also been shown in the recent work of Hou et al. [57] investigating the immiscibility of an Fe-rich melt in presence of H_2O.

4.2. Peculiar H_2O dissolution mechanisms in Fe-rich basalt

Previous spectroscopic investigations [13, 45, 46, 54] have shown that H_2O can dissolve in silicate glasses as two main species: 1) hydroxyl groups (i.e., OH) or 2) molecular H_2O (i.e., H_2O_{mol}). At low H_2O content, OH is the predominant species to be formed in silicate glasses owing to the water dissociation reaction:

(3) $H_2O^{melt} + O^{2-} \rightarrow 2OH^{-\,melt}$

This dissolution mechanism induces a depolymerization of the silicate network through the formation of silanol groups (SiOH):

(4) $Si - O - Si + H_2O^{fl} \rightarrow 2\,SiOH$

At higher H_2O content, H_2O_{mol} becomes the dominant species whereas OH remains almost constant. An additional H_2O dissolution mechanism has been inferred in recent studies based on Raman and NMR spectroscopic results [46, 58] and corresponds to the formation of Free OH groups. It has been suggested that the formation of Free OH will induce a polymerization of the silicate melt structure as the network modifying cation charges are consumed by the OH^- negative charges according to the following equation (5):

(5) $2Si - O^- M^{n+} + H_2O^{fluid} \rightarrow Si - O - Si + M^{n+}OH^n$

With M for cations (i.e., Ca, Mg, Fe) and n representing the charge of the cation.

A shoulder at 3660 cm^{-1} corresponding to Free OH vibrations [45-47] is observed for the Fe-rich glass (CL-3H-6h) and the water-rich terrestrial analogue (PR-6Hb) in Fig. 1B. Coupled with the shoulder at 3660 cm^{-1}, a peculiar peak at 670 cm^{-1} has been detected for those two spectra (Fig. 1A) with a Lorentzian shape. The occurrence of the 3660 and 670 cm^{-1} peaks appear correlated, although the assignment of the 670 cm^{-1} peak to a peculiar vibration remains to be determined. In the study of Di Genova et al. [42], Raman spectra acquired on Fe-rich basaltic glasses exhibit a specific peak at ~690 cm^{-1} that is correlated with nanolite particles due

to high Fe content, but also due to high H_2O content. Furthermore, we have noticed that some other experiments showed the same peaks: GC-H_2O-chiller, GC-H_2O-4h and GCD-3H-6h-1.5GPa.

To determine the proportion of the 3660 cm^{-1} peak, we carried out spectrum simulation using 4 peaks: 3 Gaussians and one Voigt (combination of a Gaussian and a Lorentzian component). Values of simulations are reported in the Supporting Information in Table S2. Typical simulations for PR-6Hb and CL-3H-6h are shown in Fig. 4. In the simulations in Fig. 4, CL-3H-6h sample exhibits ~17 % of Free OH and only 2 % is calculated for PR-6Hb.

In Fig. 5A, we have reported the proportions of Free OH as a function of the proportion of the 670 cm^{-1} peak (i.e., 670* corresponding to the ratio between the 670 cm^{-1} area and the total area of H_2O) for the samples: CL-3H-6h,PR-6Hb, GC-H_2O-chiller, GC-H_2O-4h and GCD-3H-6h-1.5GPa. Each data reported in this graph corresponds to the proportion determined from the simulation of a given spectrum. In Fig. 5A, we observe a correlation between the percentage of Free OH and the 670 cm^{-1} peak. The increase of the 670 cm^{-1} is correlated to an increase in Free OH. For PR-6Hb, we measure the 670*= 6 % and Free OH= 2 %. For CL-3H-6h, we obtain 670* ~60 % and 20 % of Free OH.

In Fig. 5B, the Free OH percentages are represented against the FeO_{tot}. The Free OH fraction appears also correlated to the FeO_{tot} in the sample. The Fe-rich sample, CL-3H-6h with 16.0 wt % FeO_{tot}, presents ~17 % of Free OH. The GC and GCD samples exhibit values from 3 to 7 % of Free OH, with ~12 and ~14 wt % FeO_{tot}, respectively. On the other hand, PR-6Hb with 4.5 wt % FeO_{tot}, shows only 2 % of Free OH.

Previous works have shown that the formation of Free OH is observed 1) when H_2O is dissolving in a strongly depolymerized composition [57], 2) with high H_2O concentrations [45], and 3) in aqueous solutions [47]. The presence of Free OH is rather surprising in Fe-rich glasses

investigated here considering that the total H_2O content dissolved does not exceed 1 wt %. One possible reason for the existence of Free OH groups in Fe-rich glasses could be ascribed to the structural role of iron within the glass. Recovered Fe-rich glasses (i.e., GC and CL) from high pressure experiments have a Fe ratio between Fe^{2+} / ∑Fe = 0.4 and 0.6, respectively (see Table 2) suggesting that Fe plays a network modifying role [59] within the glass when under its Fe^{2+} state. Although additional work is clearly needed to better characterize the correlation between the Free OH groups the Fe redox state; it is possible that Fe^{2+} has a high affinity to form isolated complexes with OH.

The observation of Free OH in Fe-rich melt at low H_2O content (~1 wt %) has implications on the mineralogical composition at the Mars surface. The formation of Free OH molecular clusters could constitute a precursor for an immiscible Fe-rich phase; in a similar manner to the immiscibility observed between carbonatite and silicate melts owing to the formation of Free carbonates [60]. Previous spatial missions identified multiple forms of Fe-oxides, mostly hematite and magnetite at the surface of Mars [61-63]. The separation of Fe-$(OH)_2$ rich phase could favor the formation of Fe-oxides by weathering of the basalt at the surface.

4.3. Evolution of the silicate network signature as a function of the Fe redox state estimation

The presence of Free OH should induce a change on the overall silicate network considering that Fe^{2+} cations are scavenged by the OH species. Therefore, the deficit of positive charges from the network modifying cations should induce an increase in the degree of polymerization according to the reaction (6):

(6) $2Q^n + Fe^{2+} + H_2O = 2\,Q^{n+1} + Fe(OH)_2$

This reaction equivalent to Eq. 5 shows that Q^n species proportions are changing due to the formation of Free OH clusters. For instance, Q^3 species should merge to form Q^4 species upon

the dissolution of water as Free OH clusters. This change is likely to be observed by Raman spectroscopy.

The HF region is a composition of several Gaussians peaks [60] referred to a Q^n species with, n the number of bridging O varying from 0 to 4. We conducted spectrum deconvolution of the HF region that are exhibited in Fig. 6. The results from the deconvolutions are reported in the Table S2 (Supporting Information). The deconvolutions of the Raman spectra for PR-6H-4h, GCD-3H-6h and CL-3H-6h (i.e. synthetic martian basalts) are reported in Fig. 6. The assignment of each Gaussian line is based on previous works [64]: Q^4 at 1080 cm^{-1}, Q^3 at ~1020 cm^{-1}, Q^2 at ~950 cm^{-1} and Q^1 at ~880 cm^{-1}.

For the PR-6H-4h sample, the deconvolution shows that the Q^3 (~1010 cm^{-1}) is the most intense peak whereas the GCD sample shows a more intense peak at lower Raman shift with the Q^2 (~950 cm^{-1}), leading to less polymerized network. Then, for the CL sample, we can see that the Q^2 peak is more intense but the Q^3 is almost at the same height.

Regarding solely at the Fe^{2+} content reported in Fig. 6, we can see an increase of the Fe^{2+} content in the melt from the PR-6H-4h toward CL-3H-6h. Indeed, if the GCD sample is the most oxidized, the bulk Fe^{2+} is higher as compared to the PR sample: 5.4 and 4.2 wt % Fe^{2+}, respectively. The presence of high Fe^{2+} content enhances the depolymerization of the structure, which is confirmed by the deconvolution of the GCD glass in Fig. 6. Then, the low content of Fe^{2+} coupled with the high SiO_2 content (> 51 wt %) of the PR-6H-4h sample enable a polymerization of the silicate glass. We can see that the iron-rich composition (CL sample) is richer in Fe^{2+} species (9.8 wt %). Hence, we expected a more depolymerized structure correlated with the high Fe^{2+} in the melt. However, the opposite behavior is observed from subsequent simulation reported in Fig. 6.

In order to discriminate the possible effect of Free OH related to Fe^{2+} on the degree of polymerization, we represent in the Fig. 7 the ratio of Q^4 over the sum of Q^n species as a function of Fe^{2+} normalized by the H_2O content. We choose to show the change in Q^4 species as this is the most polymerized unit (4 bridging oxygens) and the trend is the best obtained between the Q^n species; however, trends for the other species can be found in the Fig. S1 (Supporting information). The deconvolution of glasses obtained at all pressures associated with a relative error of 10 % are reported in Fig. 7. The Fig. 7 shows two major information. 1) Increasing Fe^{2+} in the glass induces a decrease in the fraction of Q^4 (from 0.23 to 0.16 between Fe^{2+}/H_2O ~1 to 11) and therefore a depolymerization of the glass. These results appear consistent with the suggested role of Fe^{2+} as a network modifier. 2) Free OH species have only a limited effect on the degree of polymerization for PR-6H-4h (without Free OH) and PR-6Hb (with Free OH) $Q^4/\sum Q^n$ = 0.23 and 0.26. The same applies for GCD-3H-6h without Free OH and GCD-3H-1.5G with Free OH: 0.18 and 0.19, respectively.

We expected measurable effect of Free OH with the increase of the polymerization degree observed in Fig. 6 (CL-3H-6h). Several aspects could explain the absence of effect shown in Fig. 7: 1) although the Free OH are visible in Raman spectra, their abundance is small compared to the $H_2O_{tot.}$; Thus the effect on the degree of polymerization is not visible or within error the Q^n simulation, 2) it is also possible that the Free OH species are not exclusively linked to Fe^{2+} and other cations such as Mg^{2+} and Ca^{2+} form Free OH clusters. However, the trend observed in Fig. 5B strongly favors an affinity of OH^- with Fe^{2+}.

Summary

In the present work, we have shown that Fe concentration in glass has a non-negligible effect on the H_2O dissolution within the melt structure. Increasing the Fe content appears to induce a

decrease in the H_2O dissolution. This result has major implications for Mars, notably for the transport of H_2O in Fe-rich melt from the mantle to the surface that will be less efficient than on Earth.

We inferred the formation of Free OH in Fe-rich glasses (i.e., martian basalt analogues) at relatively low H_2O content (~1 wt %) whereas such molecular groups appear at very high H_2O content for terrestrial basaltic glasses (> 6 wt %). The presence of Free OH molecular clusters seems to be dependent on the Fe content by increasing with FeO^{tot}. In detail, Free OH species are likely to be correlated to the Fe^{2+} in Fe-rich composition. Free OH are supposed to induce a polymerization effect on the silicate network; although further work is currently needed to investigate the exact molecular configuration in the surrounding of cations forming Free OH groups. The possibility for Free OH in the vicinity of Fe^{2+} cations represents a precursor for producing Fe-rich mineral phases through weathering of the erupted Fe-rich basalts, which will be consistent with Fe-oxides found at Mars surface.

Acknowledgements:

The author is thankful for the Centre National d'Etudes Spatiales (CNES), the Région Pays de la Loire and the Programme National de Planétologie for funding the present work. We also want to acknowledge the Laboratoire de Planétologie et Géodynamique, the IFREMER of Brest and the Institut des Matériaux Jean Rouxel of Nantes to allow us to perform our experiments and analyses.

References

[1] Squyres, S.W., Grotzinger, J.P., Arvidson, R.E., Bell III, J.F., Calvin, W., Christensen, P.R. et al. In Situ evidence for an ancient aqueous environment at Meridiani Planum, Mars. *Science*. **2004a**; 306, 1709-1714.

[2] Squyres, S.W., Arvidson, R.E., Bell III, J.F., Brückner, J., Cabol, N.A., Calvin, W., Carr, M.H., Christensen, P.R. et al., The Opportunity Rovers's Athena Science investigation at Meridiani Planum, Mars. *Science*. **2004b**; 303, 1698-1703.

[3] Tosca, N.J. and Knoll, A.H., Juvenile chemical sediments and the long term persistence of water at the surface of Mars. *Earth Planet. Sci. Lett*. 2009; 286, 379 – 386.

[4] Gross, S.H., McGovern, W.E., Rasool, S.I., Mars: Upper Atmosphere. *Science.* **1966**; 151, 1216-1221.

[5] Dreibus, G. and Wänke, H., Mars, a volatile-rich planet. *Meteoritics.* **1985**; 20, 367-381.

[6] Carr, M.H., Recharge of the early atmosphere of Mars by impact-induced release of CO_2. *Icarus*, **1989**; 79, 311-327.

[7] Mangold, N., and others,Classification scheme for sedimentary and igneous rocks in Gale crater, Mars. *Icarus*. **2017**; 284, 1-17.

[8] Bandfield, J.L., Hamilton, V.E., Christensen, P.R., A global view of Martian surface composition from MGS-TES. *Science*. **2000**; 287, 1626-1630.

[9] McSween, H.Y., Taylor, G.J., Wyatt, M.B., Elemental Composition of the Martian Crust. *Science*. **2009**; 324, 736-739.

[10] Baratoux, D., Toplis, M.J., Monnereau, M., Sautter, V., The petrological expression of early Mars volcanism. *J. Geophys. Res.: Planets.* **2013**; 118, 59-64.

[11] Sautter, V. and others, Magmatic complexity on early Mars as seen through a combination of orbital, in-situ and meteorite data. *Lithos*. **2016**; 254-255, 36-52.

[12] Cousin, A., Sautter, V., Payré, V., Forni, O., Mangold, N., Gasnault, O., Le Deit, L., Johnson, J., Maurice, S., Salvatore, M., Wiens, R.C., Gasda, P., Rapin, W., Classification of igneous rocks analyzed by ChemCam at Gale Crater, Mars. *Icarus*. **2017**; 288, 265-283.

[13] Dixon, J. E., & Stolper, E. M., An experimental study of water and carbon dioxide solubilities in mid-ocean ridge basaltic liquids. Part II. *J. Petrol*. **1995**; 36, 1633–1646.

[14] Morizet, Y., Paris, M., Gaillard, F., Scaillet, B., C-O-H fluid solubility in haplobasalt under reducing conditions: An experimental study. *Chem. Geol*. **2010**; 279, 1-16.

[15] Jugo, J., Luth, R.W., Richards, J.P., An experimental study of the sulfur content in basaltic melts saturated with immiscible sulfide luquids at 1300°C and 1.0 GPa. *J. Petrol*. **2005**; 46, 783 – 798.

[16] Shishkina, T. A., Botcharnikov, R. E., Holtz, F., Almeev, R. R., Jazwa, A. M., & Jakubiak, A. A., Compositional and pressure effects on the solubility of H_2O and CO_2 in mafic melts. *Chem. Geol*. **2014**; 388, 112–129.

[17] Brey, G., & Green, D. H., Solubility of CO_2 in Olivine Melilitite at High Pressures and Role of CO_2 in the Earth's Upper Mantle. *Contrib. Mineral. Petrol*. **1976**; 55, 217–230.

[18] Brooker, R. A., Kohn, S. C., Holloway, J. R., & Mcmillan, P. F., Structural controls on the solubility of CO_2 in silicate melts Part I : bulk solubility data. *Chem. Geol*. **2001**; 174, 225–239.

[19] Moussallam, Y., Morizet, Y., Massuyeau, M., Laumonier, M., Gaillard, F., CO_2 solubility in kimberlite melts. *Chem. Geol*.**2014**; 418, 198 – 205.

[20] Moussallam, Y., Morizet, Y., Gaillard, F., Unconventional H_2O-CO_2 solubility in kimberlite defines the depth of pipe root zone. *Earth Planet. Sci. Lett*. **2016**; 447, 151 – 160.

[21] Filiberto, J., Experimental constraints on the parental liquid of the Chassigny meteorite: A possible link between the Chassigny meteorite and a Martian Gusev basalt. *Geochim. Cosmochim. Acta*. **2008**; 72, 690-701.

[22] McCubbin, F. M., Hauri, E. H., Elardo, S. M., Vander Kaaden, K. E., Wang, J., & Shearer, C. K., Hydrous melting of the martian mantle produced both depleted and enriched shergottites. *Geology*. **2012**; 40, 683–686.

[23] Weis, F.A., Bellucci, J.J., Skogby, H., Stalder, R., Nemchin, A.A., Whitehouse, M.J., Water content in the Martian mantle: A Nakhla perspective. *Geochim. Cosmochim. Acta*. **2017**; 212, 84 – 98.

[24] Wadhwa, M., Redox state of Mars' upper mantle and crust from Eu anomalies in Shergottite pyroxenes. *Science*. **2001**; 23, 1527 – 1530.

[25] Herd, C.D.K., The oxygen fugacity of olivine-phyric martian basalts and the components within the mantle and crust of Mars. *Meteorit. Planet. Sci*. **2003**; 38, 1793 – 1805.

[26] Schmidt, M.E., Schrader, C.M., McCoy, T.J., The primary fO_2 of basalts examined by the Spirit rover in Gusev Crater, Mars: Evidence for multiple redox states in the martian interior. *Earth Planet. Sci. Lett*. **2013**; 384, 198 – 208.

[27] Stanley, B.D., Hirschmann, M.M., Withers, A.C., CO_2 solubility in Martian basalts and Martian atmospheric evolution. *Geochim. Cosmochim. Acta*. **2011**; 75, 5987 – 6003.

[28] Stanley, B.D., Schaub, D.R., Hirschmann, M.M., CO_2 solubility in primitive martian basalts similar to Yamato 980459, the effect of composition on CO_2 solubility of basalts, and the evolution of the martian atmosphere. *Am. Min*. **2012**; 97, 1841 – 1848.

[29] Stanley, B.D., Hirschmann, M.M., Withers, A.C. (2014): Solubility of C-O-H volatiles in graphite-saturated martian basalts. Geochim. Cosmochim. Acta, 129, 545 – 76.

[30] Armstrong, L.S., Hirschmann, M.M, Stanley, B.D., Falksen, E.G., Jacobsen, S.D., Speciation and solubility of reduced C-O-H-N volatiles in mafic melts: Implications for volcanism, atmospheric evolution, and deep volatile cycles in the terrestrial planets. *Geochim. Cosmochim. Acta.* **2015**; 171, 283 – 302.

[31] Médard, E., Grove, T. L., Early hydrous melting and degassing of the Martian interior. *J. Geophys. Res.:Planets*. **2006**; 111, E11003.

[32] McCubbin, F.M., Nekvasil, H., Harrington, A.D., Elardo, S.M., Lindsley, D.H., Compositional diversity and stratification of the Martian crust: Inferences from crystallization experiments on the picrobasalt Humphrey from Gusev Crater, Mars. *J. Geophys. Res*. **2008**; 113, 1 – 16.

[33] Nekvasil, H., McCubbin, F.M., Harrington, A., Elardo, S., Lindsley, D.H., Linking the Chassigny meteorite and the Martian surface rock Backstay: Insights into igneous crustal differenciation processes on Mars. *Meteorit. Planet. Sci*. **2009**; 44, 853 – 869.

[34] Noguchi, N., Shinoda, K., and Masuda, K., Quantitative analysis of binary mineral mixtures using Raman microspectroscopy: Calibration curves for silica and calcium carbonate minerals and application to an opaline silica nodule of volcanic origin. *J. Mineral. Petrol. Sci*. **2009**; 104, 253-262.

[35] Kristova, P., Hopkinson, L., Rutt, K., Hunter, H., Cressey, G., Quantitative analyses of powdered multi-minerallic carbonate aggregates using a portable Raman spectrometer. *Am. Min*. **2013**; 98, 401- 409.

[36] Larre, C., Morizet, Y., Guillot-Deudon, C., Baron, F., Mangold, N., Quantitative Raman calibration of sulfate-bearing polymineralic mixtures: a S quantification in sedimentary rocks on Mars. *Min. Mag*. **2018**; 1-38.

[37] Morizet, Y., Brooker, R.A., Iacono-Marziano, G., Kjarsgaard, B.A., Quantification of dissolved CO_2 in silicate glasses using micro-Raman spectroscopy. *Am. Min*. **2013a**; 98, 1788-1802.

[38] Morizet, Y., Gennaro, E., Jego, S., Zajacz, Z., Iacono-Marziano, G., Pichavant, M., Di Carlo, I., Ferraina, C., Lesne, P., A Raman calibration for the quantification of SO_4^{2-} groups dissolved in silicate glasses: Application to natural melt inclusions. *Am. Min*. **2017a**; 102, 2065-2076.

[39] Zajacz, Z., Halter, W., Malfait, W.J., Bachmann, O., Bodnar, R.J., Hirschmann, M.M., Mandeville, C.W., Morizet, Y., Müntener, O., Ulmer, P., Webster, J.D., A composition-

552 independent quantitative determination of the water content in silicate glasses and silicate melt
553 inclusions by confocal Raman spectroscopy. *Contrib. Mineral. Petrol*. **2005**; 150, 631-642.

554 [40] Behrens, H., Roux, J., Neuville, D. R., & Siemann, M., Quantification of dissolved H_2O
555 in silicate glasses using confocal microRaman spectroscopy. *Chem. Geol*, **2006**; 229, 96–112.

556 [41] Mercier, M., Di Muro, A., Giordano, D., Métrich, N., Lesne, P., Pichavant, M., Scaillet,
557 B., Clocchiatti, R., Montagnac, G., Influence of glass polymerization and oxidation on micro-
558 Raman water analysis in alumino-silicate glasses. *Geochim. Cosmochim. Acta*.**2009**; 73, 197-
559 217.

560 [42] Di Genova, D., Sicola, S., Romano, C., Vona, A., Fanara, S., Spina, L., Effect of iron and
561 nanolites on Raman spectra of volcanic glasses: A reassessment of existing strategies to
562 estimate the water content. *Chem. Geol*. **2017**; 475, 76-86.

563 [43] Schiavi, F., Bolfan-Casanova, N., Withers, A.C., Médard, E., Laumonier, M., Laporte, D.,
564 Flaherty, T., Gomez-Ulla, A., Water quantification in silicate glasses by Raman spectroscopy:
565 Correcting for the effects of confocality, density and ferric iron. *Chem. Geol*. **2018**; 483, 312 –
566 331.

567 [44] Kägi, R., Müntener, O., Ulmer, P., Ottolini, L., Piston-cylinder experiments of H_2O
568 undersaturated Fe-bearing systems: An experimental setup approaching fO_2 conditions of
569 natural calc-alkaline magmas. *Am. Min*. **2005**; 90, 708 – 717.

570 [45] Mysen, B.O. and Virgo, D., Volatiles in silicate melts at high pressure and temperature:
571 interaction between OH groups and Si^{4+}, Al^{3+}, Ca^{2+}, Na^{+} and H^{+}. *Chem. Geol*. **1986**; 57, 303-
572 331.

[46] Mysen, B.O. and Cody, G.D., Solution mechanisms of H_2O in depolymerized peralkaline melts. *Geochim. Cosmochim. Acta*. **2005**; 69, 5557 – 5566.

[47] Corridoni, T., Sodo, A., Bruni, F., Ricci, M.A., Nardone, M., Probing water dynamics with OH^-. *Chem. Phys. 2007*; 336, 183-187.

[48] Brugier, Y.-.A., Alletti, M., Pichavant, M., Fe pre-enrichment: A new method to counteract iron loss in experiments on basaltic melts. *Am. Min*. **2015**; 100, 2106 – 2111.

[49] Wilson, A.D., The micro-determination of Fe^{2+} in silicate minerals by a volumetric and a colorimetric method. *Analyst*. **1960**; 85, 823 – 827.

[50] Schuessler J.A., Botcharnikov R.E., Behrens H., Misiti V. and Freda C., Oxidation state of iron in hydrous phono-tephritic melts. *Am. Min*. **200**8; 93, 1493-1504.

[51] Govindaraju, K., 1994 Compilation of working values and sample description for 383 geostandards. *Geostand. Newsl*. **1994**; 18, 1 – 158.

[52] McMillan, P. and Piriou, B., The structures and vibrational spectra of crystals and glasses in the silica-alumina system. *J. Non-Cryst. Solids*. **1982**; 53, 279-298.

[53] Freund, F., Wengeler, H., Kathrein, H., Knobel, R., Oberheuser, G., Maiti, G.C., Reil, D., Knipping, U., Kötz, J., Hydrogen and carbon derived from dissolved H_2O and CO_2 in minerals and melts. *Bull. Mineral*. **1982**; 106, 185 – 200.

[54] Ohlhorst, S., Behrens, H., Holtz, F., Compositional dependence of molar absorptivities of near-infrared OH- and H_2O bands in rhyolitic to basaltic glasses. *Chem. Geol*. **2001**; 174, 5 – 20.

[55] Stolper, E., Water in silicate glasses: An infrared spectroscopic study. *Contrib. Mineral. Petrol*. **1982**; 81, 1 – 17.

[56] Newman, S. and Lowenstern, J.B., VolatileCalc: a silicate melt-H_2O-CO_2 solution model written in Visual Basic for excel. *Comput. Geosci*. **2001**; 28, 597 – 604.[57] Papale, P., Modeling of the solubility of a two-component H_2O + CO_2 fluid in silicate liquids. *Am. Min*. **1999**; 84, 477 – 492.

[57] Hou, T., Charlier, B., Holtz, F., Veksler, I., Zhang, Z., Thomas, R., Namur, O., Immiscible hydrous Fe-Ca-P melt and the origin of iron oxide-apatite ore depostits. *Nat. Commun*. **2018;** 9, 1-8.

[58] Xue, X., and Kanzaki, M., Dissolution mechanisms of water in depolymerized silicate melts: Constraints from ^{1}H and ^{29}Si NMR spectroscopy and ab initio calculations. *Geochim. Cosmochim. Acta.* **2004**; 68, 5027 – 5057.

[59] Mysen B.O. Relations between Structure, Redox, Equilibria of Iron, and Properties of Magmatic Liquids. *Adv. Phys. Geochem*. **1991**; 9, 41-98.

[60] Morizet, Y., Florian, P., Paris, M., Gaillard, F., O^{17} NMR evidence of free ionic clusters M^{n+} CO_3^{2-} in silicate glasses: Precursors for carbonate-silicate liquids immiscibility. *Am. Min.* **2017b**; 102, 1561 – 1564.

[61] Morris, R.V. et al., Mineralogy at Gusev Crater from the Mössbauer Spectrometer on the Spirit Rover. *Science*. **2004**; 305, 833 – 836.

[62] Bribing, J.-P., Langevin, Y., Mustard, J.F., Poulet, F., Arvidson, R., Gendrin, A., Gondet, B., Mangold, N., Pinet, P., Forget, F. and the OMEGA team, Global mineralogical and aqueous Mars history derived from OMEGA/Mars Express Data. *Science*. **2006**; 312, 400 – 403.

[63] Le Deit, L., Le Mouélic, S., Bourgeois, O., Combe, J.-P., Mège, Sotin, C., Gendrin, A., Hauber, E., Mangold, N., Bribing J.-P., Ferric oxides in East Candor Chasma, Valles Marineris (Mars) inferred from analysis of OMEGA/Mars Express data : Identification and geological interpretation. *J. Geophys. Res*. **2008**; 113, 1 – 18.

[64] Mysen, B.O., Virgo, D., Seifert, F.A., The structure of silicate melts: implications for chemical and physical properties of natural magma. *Rev. Geophys. Space Phys*. **1982**; 20, 353 – 383.

Tables:

Table 1: Starting compositions for PR (natural glass of Popping Rock) an Earth basalt analogue, CL and GC synthetic martian basalts.

Oxides (wt %)	PR [a]	GC [b]	CL [b]
SiO_2	50.3	48.1	46.5
TiO_2	1.8		
Al_2O_3	14.8	10.2	8.2
FeO	8.8	15.5	23.5
Fe_2O_3	1.3		
MnO	0.2		
MgO	7.7	13.1	9.8
CaO	10.8	8.1	7.6
Na_2O	2.9	4.9	4.3
K_2O	0.7		
P_2O_5	0.3		
Total	99.6	100.0	100.0
NBO/T [c]	0.38	0.56	0.33
$\frac{Fe^{2+}}{\sum Fe}$ [d]		0.03 *(1)*	0.02 *(1)*

Notes :
[a] Natural glass of Popping Rock
[b] Synthetic analogues to Martian basalt (> 15 wt % FeO)
[c] Calculated on the basis of Fe in its tetrahedral coordination (i.e. Fe^{3+}), acting as a network former like Si, Al and Ti tetrahedron. NBO/T parameter ranging from 0 to 4. Calculations made on an anhydrous basis
[d] $\frac{Fe^{2+}}{\sum Fe}$ Ratio calculated from wet chemistry analyses for decarbonated powders. Standards errors (1 σ) are reported in brackets at 10^{-2}

Samples	GC-H_2O-chiller	GC-H_2O-4h	GC-3H-6h	GC-1H-4h	GCD-3H-6h	GCD-3H-6h-1.5GPa	GCD-2H-0.5GPa [a]	CL-3H-6h	PR-3H-6h	PR-6H-4h	PR-6Hb [a]
H_2O^{ini} (wt %)	2.6	2.6	2.4	0.9	2.7	3.0	1.9	2.9	2.9	5.7	6.5
CO_2^{ini} (wt %)	3.5	3.5	3.5	3.5				3.1			
P (GPa)	1	1	1	1	1	1.5	0.5	1	1	1	1
T (°C)	1600	1600	1600	1600	1600	1600	1600	1600	1600	1600	1500
t (h)	1	4	6	4	6	6	6	6	6	4	1
SiO_2	48.6 *(8)*	50.1 *(3)*	50.9 *(3)*	51.1 *(3)*	48.5 *(2)*	47.8 *(4)*	49.4 *(2)*	50.9 *(2)*	54.8 *(3)*	51.2 *(3)*	51.14 *(20)*
TiO_2									1.9 *(1)*	1.7 *(1)*	1.51 *(6)*
Al_2O_3	11.5 *(5)*	10.7 *(4)*	10.8 *(2)*	10.6 *(2)*	10.2 *(2)*	10.4 *(20)*	10.9 *(1)*	8.7 *(2)*	15.2 *(3)*	14.5 *(3)*	14.49 *(11)*
FeO_{tot}	13.4 *(4)*	12.1 *(3)*	10.6 *(3)*	11.6 *(3)*	14.2 *(3)*	14.1 *(3)*	13.4 *(1)*	16.0 *(4)*	2.7 *(1)*	5.8 *(2)*	4.54 *(11)*
MnO									0.1 *(0)*	0.1 *(0)*	0.11 *(2)*
MgO	12.7 *(1.0)*	12.7 *(4)*	12.8 *(3)*	12.9 *(3)*	12.3 *(3)*	12.0 *(3)*	11.3 *(1)*	10.0 *(1)*	7.9 *(2)*	7.4 *(2)*	8.45 *(21)*
CaO	5.9 *(1)*	5.6 *(3)*	5.9 *(2)*	6.0 *(1)*	6.9 *(3)*	6.6 *(2)*	7.6 *(1)*	5.6 *(2)*	10.7 *(2)*	10.1 *(3)*	10.71 *(18)*
Na_2O	3.6 *(3)*	4.0 *(6)*	4.3 *(2)*	4.5 *(1)*	4.2 *(3)*	3.7 *(3)*	5.1 *(1)*	4.0 *(2)*	3.0 *(1)*	2.5 *(1)*	3.13 *(5)*
K_2O									0.7 *(0)*	0.7 *(0)*	0.61 *(3)*
P_2O_5									0.3 *(1)*	0.3 *(1)*	0.26 *(3)*
Total	95.6	95.2	95.3	96.8	96.4	94.7	97.8	95.3	95.2	92.8	93.61
H_2O_{final} (wt %)	1.0 *(1)*	1.0 *(2)*	1.5 *(1)*	0.8 *(1)*	0.7 *(1)*	0.8 *(1)*	0.9 *(1)*	0.9 *(2)*	2.7 *(2)*	4.1 *(2)*	6.5 (3)
Free OH (%)	6.0	3.0				6.6		17.1			2.0
$\frac{Fe^{2+}}{\sum Fe}$ [b]	0.47	0.49	0.53	0.57	0.37	0.46	0.44	0.58	0.83	0.70	0.82

Notes:

[a] Final chemical compositions determined by SEM only

[b] $\frac{Fe^{2+}}{\sum Fe}$ Ratio calculated from wet chemistry analyses

Table 2: Experimental settings for the different samples (P, T, t, H_2O content). Chemical compositions of the samples determined by EPMA and SEM analyses. Final content of H_2O and FeO_{tot} are also reported, associated with wet chemistry results. The Free OH percentages are added for samples presenting the features at 3660 cm^{-1}. The calculation of Free OH percentages is made on the deconvolution of the H_2O area. Detailed of deconvolutions are reported in the Table S2 (Supporting Information). Standards errors (1 σ) are reported in brackets at 10^{-1}. The associated standard errors of wet chemistry measurements are 0.01.

Supporting Information Tables:

	PR-3H-6h	PR-6H-4h	PR-6Hb	GC-3H-6h	GC-1H-4h	GCD-3H-6h
ε_{4500} *	0.56 [a]	0.56	0.56	0.98 [b]	0.98	0.98
ε_{5200}	0.56	0.56	0.56	1.76	1.76	1.76
Density ** (g/L)	2789	2765	2722	2815	2832	2833
H_2O wt % (FTIR)	3.6 *(3)*	6.1 *(9)*	6.9 *(4)*	1.4 *(2)*	1.0 *(3)*	0.8 *(2)*
			H_2O from Raman spectroscopy (% wt):			
Mercier et al. [41]	2.7 *(2)*	4.1 *(2)*	6.5 *(3)*	1.5 *(1)*	0.8 *(1)*	0.7 *(1)*
Behrens et al. [40]	2.2 *(1)*	5.0 *(1)*	8.1 *(4)*	2.3 *(1)*	1.1 *(1)*	1.1 *(1)*
Schiavi et al. [43]	1.4 *(1)*	3.0 *(1)*	4.9 *(3)*	1.4 *(2)*	0.7 *(2)*	0.7 *(2)*

Notes :
* : extinction coefficient L/mol/cm
** : calculated according to Schiavi et al. [43]
[a]: From Ohlhorst et al. [54]
[b]: From Stolper [55]

Table S1: FTIR and Raman H_2O quantifications. Description of the parameters chosen for FTIR calculations.

673

			GC-H_2O-chiller	GC-H_2O-4h	GC-3H-6h	GC-1H-4h	GCD-3H-6h	GCD-3H-6h-1.5G	GCD-2H-0.5G	CL-3H-6h	PR-3H-6h	PR-6H-4h	PR-6Hb
HF region	Q1	Position (cm^{-1})	884	887	874	886	877	882	875	882	879	885	905
		FWHM	80	81	82	78	78	82	77	84	84	79	70
		Area %	20	20	18	20	22	20	18	20	15	15	14
	Q2	Position (cm^{-1})	948	951	940	951	940	946	940	947	951	950	969
		FWHM	82	86	81	83	87	87	76	83	78	82	69
		Area %	33	32	32	32	33	32	34	34	26	28	31
	Q3	Position (cm^{-1})	1011	1014	1001	1012	1001	1009	999	1011	1007	1005	1020
		FWHM	82	88	90	82	94	87	81	83	74	77	66
		Area %	29	29	29	28	27	29	29	31	32	34	31
	Q4	Position (cm^{-1})	1079	1082	1073	1081	1072	1076	1065	1075	1077	1077	1078
		FWHM	86	91	90	83	90	90	79	84	72	83	63
		Area %	19	20	21	19	18	19	19	16	25	23	26
H_2O region	D1	Position (cm^{-1})	3357	3252	3278	3380	3323	3374	3398	3477	3410	3278	3279
		FWHM	208	200	222	219	126	284	126	220	201	356	228
		Area %	16	23	16	28	40	20	18	28	42	24	19
	D2	Position (cm^{-1})	3473	3478	3391	3480	3446	3514	3558	3590	3573	3447	3459
		FWHM	146	220	109	129	122	160	137	130	149	176	184
		Area %	30	40	23	31	50	32	82	55	58	32	29
	D3	Position (cm^{-1})	3581	3590	3556	3596	3571	3606				3576	3586
		FWHM	130	130	179	116	133	130				141	148
		Area %	48	34	61	41	10	42				44	50
	Free OH	Position (cm^{-1})	3666	3672				3673		3661			3665
		FWHM	52	50				48		54			43
		Area %	6	3				7		17			2

674

675 Table S2: Deconvolution results for each sample in the HF (800 – 1250 cm^{-1}) region and the H_2O region (3000 – 4000 cm^{-1}). For each deconvolution, the

676 position peak is first described, then the FWHM (i.e., Full Width at Half Maximum) and the area percentage (area %). The addition of D1 to D3 coupled with

677 the Free OH peak represents the entire H_2O vibration.

Figure captions

Fig. 1: A) Raman spectra of the 200 – 1250 cm^{-1} region for the Fe-poor glasses (PR) and the synthetic Fe-rich glasses obtained at 1 GPa. B) Raman spectra of the same samples in the high frequency region (2600 – 4000 cm^{-1}). Spectra are ranked according to the FeO_{tot} content in the samples. Spectra are normalized to the most intense peak (arbitrary units).

Fig. 2: H_2O quantifications by FTIR against calibrations established by Raman spectroscopy for Mercier et al. [41] in black, Behrens et al. [40] in blue and Schiavi et al. [43] in green. Error bars reported are the error from the homogenization of the sample when it is above the calibration error of each study.

Fig. 3: H_2O dissolved in the melt versus the FeO_{tot} measured by EPMA analysis in our samples at 1 GPa. The H_2O^{ini} content is also reported.

Fig. 4: Deconvolution of the H_2O region (2600 – 4000 cm^{-1}) for CL-3H-6h and PR-6Hb samples. In blue is highlighted the Free OH area. The CL-3H-6h sample has been increased x5 for clarity.

Fig. 5: A) Percentage of Free OH (i.e., A_{3660}/A_{H2Otot} ; with A the area from deconvolution of the 3660 cm^{-1} and the water band from 3000 to 4000 cm^{-1}) versus the percentage of the 670 cm^{-1} peak (i.e., 670*) normalized by the total H_2O area (A_{H2Otot}); B) Free OH percentages in function of the total iron content (FeO_{tot}).

Fig. 6: Deconvolution of the high frequency region (i.e., HF; silicate matrix signal) for CL-3H-6h, GCD-3H-6h and PR-6H-4h. Gaussian lines are in green, cumulative peaks of the Gaussian lines are the black and the residuals from simulations is the black dotted lines. H_2O and FeO_{tot} final content for each experiment are localized next to their respective spectrum. The Fe^{2+} content is given for each sample. Spectra are normalized to the most intense peak (arbitrary units).

Fig. 7: Ratio of $Q^4/\sum Q^n$ species versus the Fe^{2+} normalized by the H_2O content for all samples. PR samples are in green, where synthetic Fe-rich experiments are represented in red. The black stars are samples presenting Free OH molecular groups. A relative error of 10 % has been applied.

Supporting Information Figure:

Fig. S1: Ratio of the Q^n species in function of the Fe^{2+} normalized by the H_2O content for PR glasses (i.e., Fe-poor) in green, GC/CL samples (Fe-rich synthetic glasses) in red, and the glasses presenting Free OH molecular groups in black stars: A) $Q^1/\sum Q^n$, B) $Q^2/\sum Q^n$ and C) $Q^3/\sum Q^n$. A relative error of 10 % on the deconvolution is applied.

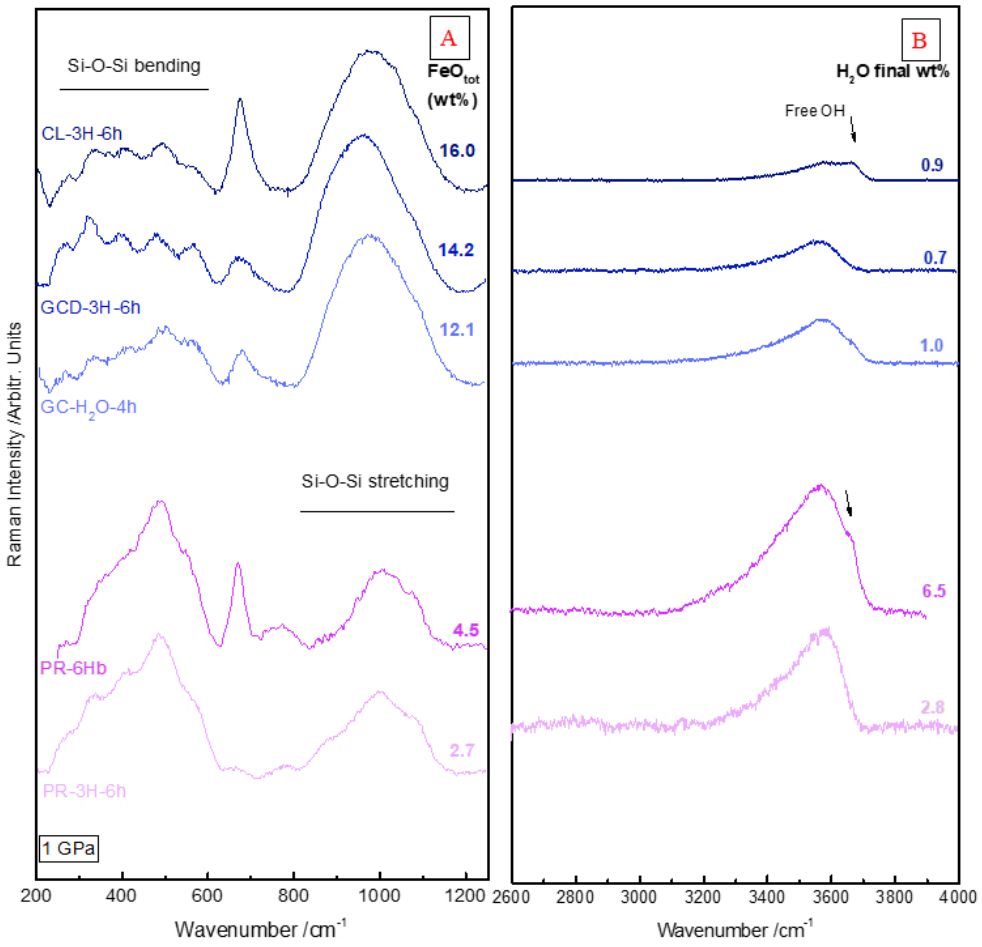

Fig. 1: A) Raman spectra of the 200 – 1250 cm-1 region for the Fe-poor glasses (PR) and the synthetic Fe-rich glasses obtained at 1 GPa. B) Raman spectra of the same samples in the high frequency region (2600 – 4000 cm-1). Spectra are ranked according to the FeOtot content in the samples. Spectra are normalized to the most intense peak (arbitrary units).

202x190mm (96 x 96 DPI)

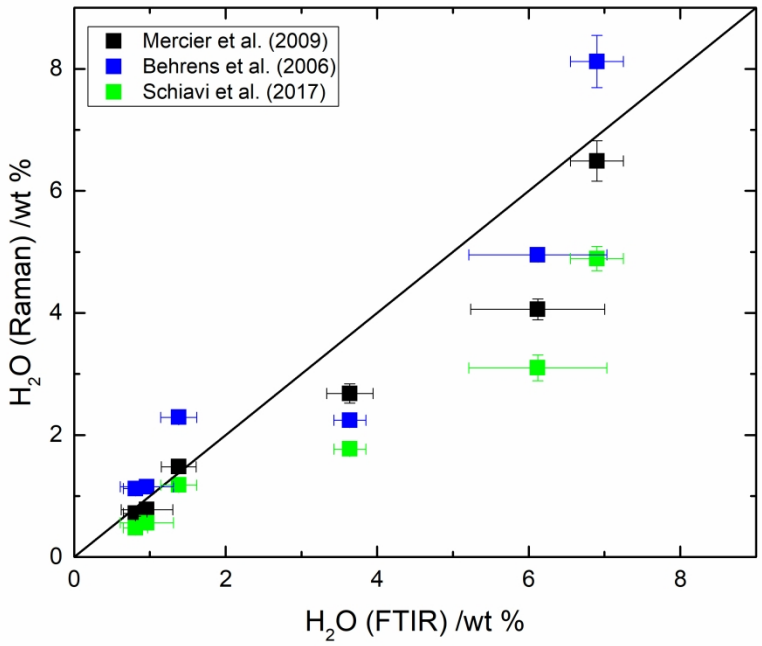

Fig. 2: H2O quantifications by FTIR against calibrations established by Raman spectroscopy for Mercier et al. [41] in black, Behrens et al. [40] in blue and Schiavi et al. [43] in green. Error bars reported are the error from the homogenization of the sample when it is above the calibration error of each study.

272x208mm (300 x 300 DPI)

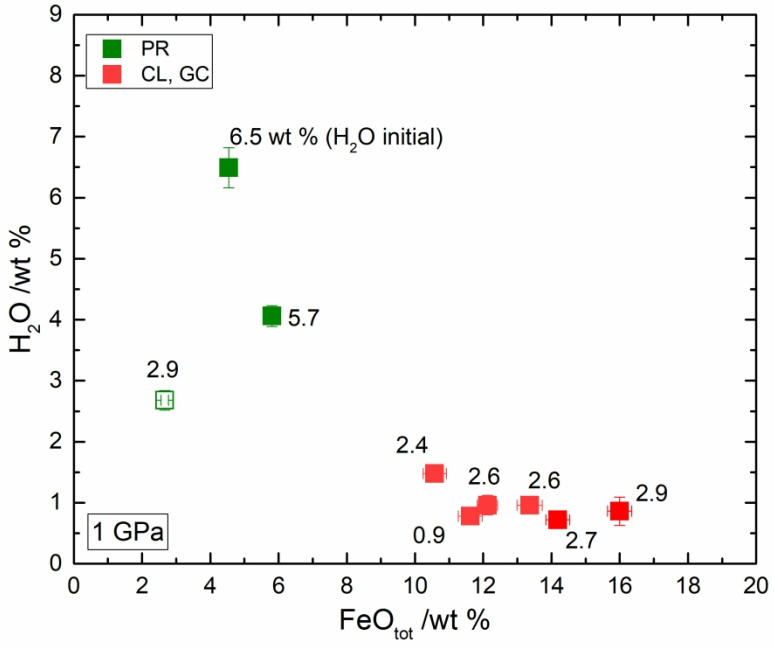

Fig. 3: H2O dissolved in the melt versus the FeOtot measured by EPMA analysis in our samples at 1 GPa. The H2Oini content is also reported.

272x208mm (300 x 300 DPI)

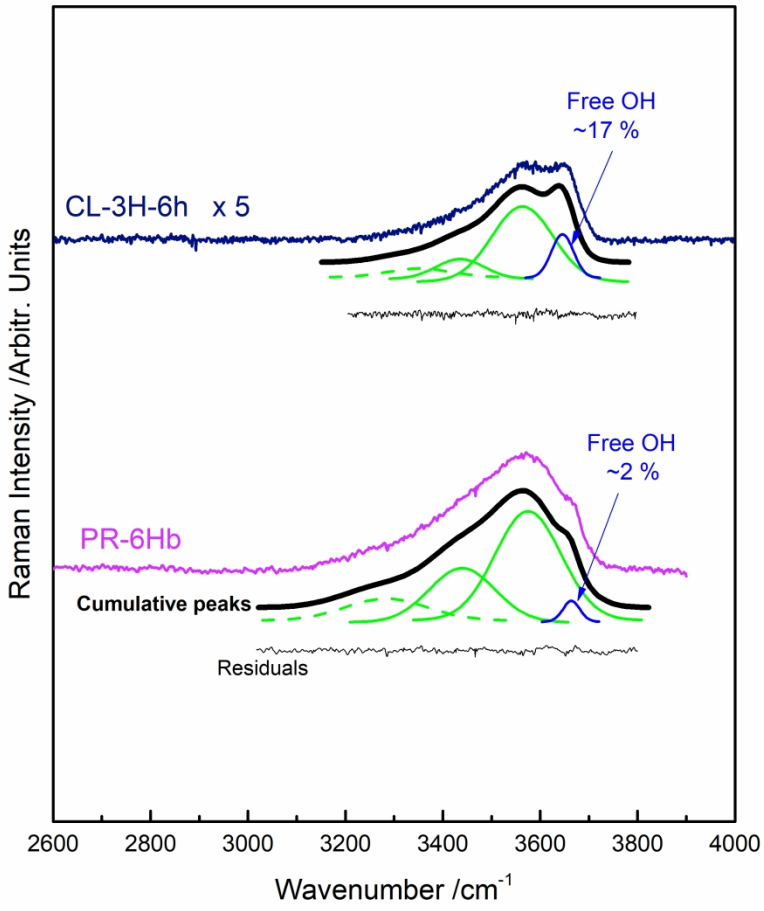

Fig. 4: Deconvolution of the H2O region (2600 – 4000 cm-1) for CL-3H-6h and PR-6Hb samples. In blue is highlighted the Free OH area. The CL-3H-6h sample has been increased x5 for clarity.

272x308mm (300 x 300 DPI)

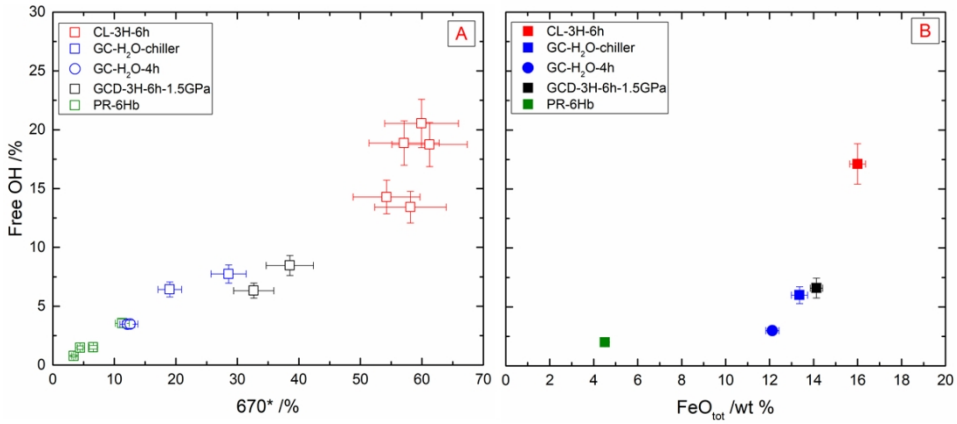

Fig. 5: A) Percentage of Free OH (i.e., A3660/AH2Otot ; with A the area from deconvolution of the 3660 cm-1 and the water band from 3000 to 4000 cm-1) versus the percentage of the 670 cm-1 peak (i.e., 670*) normalized by the total H2O area (AH2Otot); B) Free OH percentages in function of the total iron content (FeOtot).

338x190mm (96 x 96 DPI)

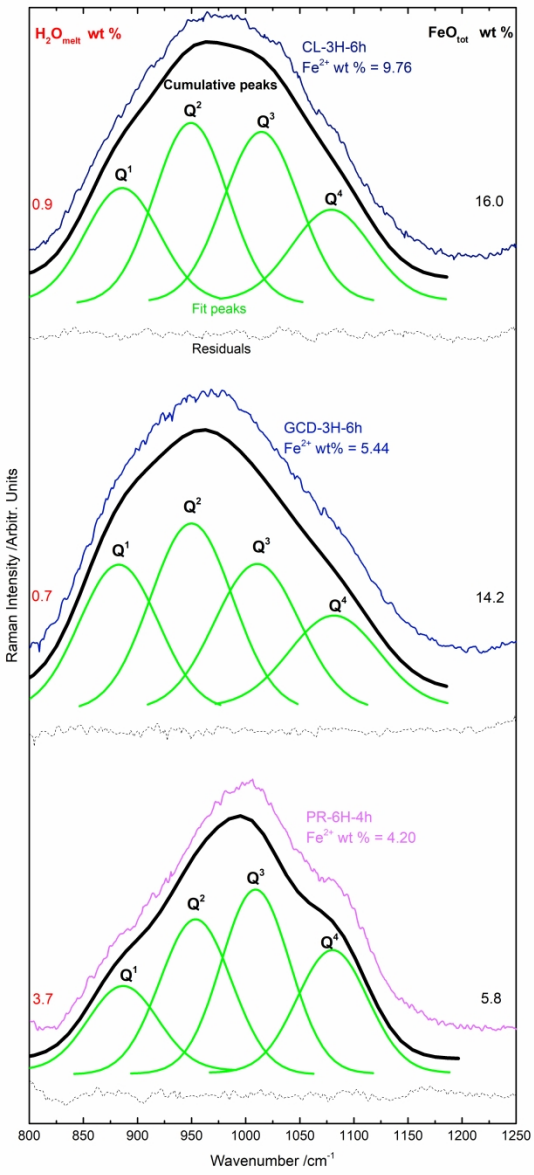

Fig. 6: Deconvolution of the high frequency region (i.e., HF; silicate matrix signal) for CL-3H-6h, GCD-3H-6h and PR-6H-4h. Gaussian lines are in green, cumulative peaks of the Gaussian lines are the black and the residuals from simulations is the black dotted lines. H2O and FeOtot final content for each experiment are localized next to their respective spectrum. The Fe2+ content is given for each sample. Spectra are normalized to the most intense peak (arbitrary units).

289x624mm (300 x 300 DPI)

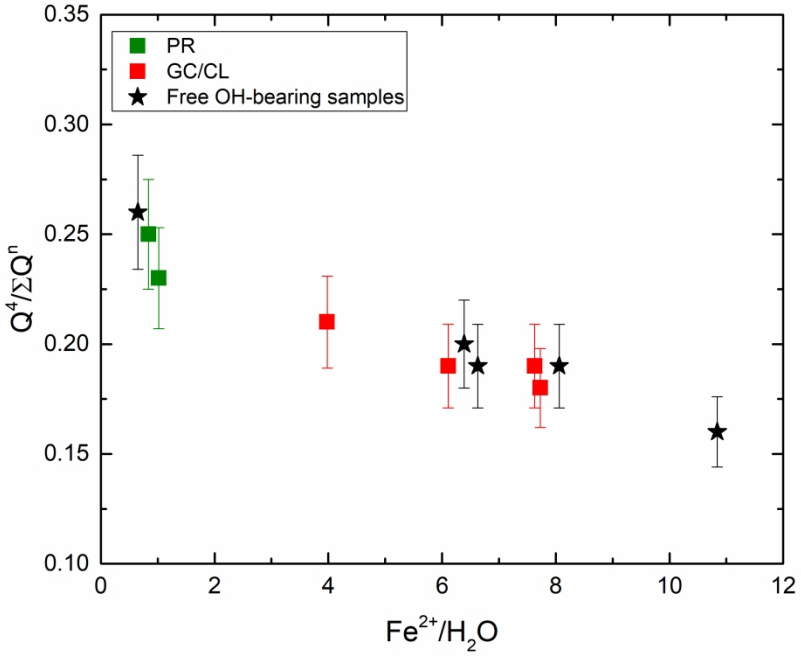

Fig. 7: Ratio of Q4/ΣQn species versus the Fe2+ normalized by the H2O content for all samples. PR samples are in green, where synthetic Fe-rich experiments are represented in red. The black stars are samples presenting Free OH molecular groups. A relative error of 10 % has been applied.

272x208mm (300 x 300 DPI)

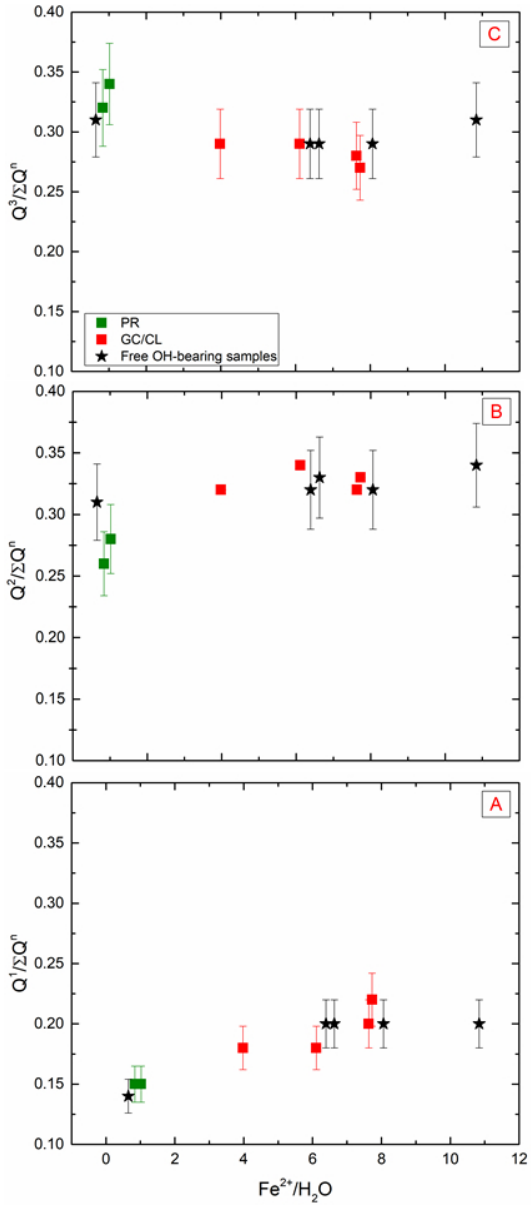

Fig. S1: Ratio of the Qn species in function of the Fe2+ normalized by the H2O content for PR glasses (i.e., Fe-poor) in green, GC/CL samples (Fe-rich synthetic glasses) in red, and the glasses presenting Free OH molecular groups in black stars: A) Q1/ΣQn, B) Q2/ΣQn and C) Q3/ΣQn. A relative error of 10 % on the deconvolution is applied.

117x254mm (96 x 96 DPI)